Materials Science & Engineering A 855 (2022) 143882

Contents lists available at ScienceDirect

Materials Science & Engineering A

journal homepage: www.elsevier.com/locate/msea

Strain hardening in twinning-induced plasticity stainless steel produced by laser powder bed fusion

Hossein Eskandari Sabzi [a], Xiao-Hui Li [b], Chi Zhang [c], Hanwei Fu [b,*], Pedro E.J. Rivera-Díaz-del-Castillo [a,*]

[a] Department of Engineering, Engineering Building, Lancaster University, LA1 4YW, United Kingdom
[b] School of Materials Science and Engineering, Beihang University, No. 37 Xueyuan Road, Beijing, 100191, China
[c] Key Laboratory of Advanced Materials of Ministry of Education, School of Materials Science and Engineering, Tsinghua University, Beijing, 100084, China

ARTICLE INFO

Keywords:
Laser powder bed fusion
Additive manufacturing
316L stainless steel
Strain hardening
Twinning-induced plasticity
Residual stress

ABSTRACT

A modelling approach is presented to identify the deformation mechanisms of 316L stainless steel produced by laser powder bed fusion (LPBF). The approach incorporates the evolution of dislocations, forming a forest, and of twins, which develop a back-stress. The overall plasticity behaviour is described in terms of dislocation multiplication and annihilation progress with strain. The modelling is matched up with detailed electron microscopy observations; the combination of both demonstrates the deformation behaviour of LPBF builds is intrinsically different to that of wrought alloys. LPBFed samples undergo three stages of deformation, with the first developing twins, which formation quickly saturates; the second sees a dramatic increase in dislocation forest hardening, combined with dislocation recovery; and the third undergoes dynamic recrystallisation taking place around heavily twinned sections. Opposite to wrought alloys, LPBFed specimens decrease their density of statistically stored dislocations throughout deformation, and it is shown that this behaviour is replicated by other LPBFed metals, including high-entropy alloys. The intrinsic behavioural differences in LPBF plasticity is thought to be due to the presence of a residual stress; this promotes dislocation recovery from the onset of deformation.

1. Introduction

Determining the strain hardening mechanisms of engineering alloys produced by additive manufacturing (AM) is a topic of fundamental importance in metallurgy. By producing effective barriers against dislocation glide, twinning-induced plasticity (TWIP) and transformation-induced plasticity (TRIP) are amongst the most important deformation mechanisms to improve strain hardening in low stacking fault energy (SFE) face-centred cubic (FCC) metals and alloys [1,2]. Recently, it has been discovered that laser powder bed fusion (LPBF) AM can be used to produce low SFE FCC builds with outstanding mechanical properties such as yield strength, while maintaining a similar ductility to their wrought counterparts [3]. Of the low SFE austenitic steels (SSs), LPBFed 316L SS has frequently been studied due to its ability to be printed without severe defects such as cracks and porosity (printability), and a significant increase in yield strength values in the as-built state [4,5]. There have been several models to predict yield strength of LPBFed 316L SS [4,6–8]. Chen et al. [9] used crystal plasticity finite element method to simulate tension–compression asymmetry of yield strength and strain hardening of an LPBFed 316L SS. They have found that residual stresses and associated back-stress arised from the dislocation distributions influence the strain hardening behaviour. However, a unified strain hardening model that can describe the distinctive deformation mechanisms of LPBFed 316L SS is lacking.

New experimental investigations have revealed that room temperature deformation mechanisms of LPBFed 316L SS include dislocation slip, TWIP, and dynamic recrystallisation (DRX) [10–12], whereas wrought 316L SS is strengthened by dislocation slip, TWIP and TRIP effects, without any report of DRX [13,14]. This difference in strain hardening mechanisms stems from the austenite stability, which is controlled by dislocation density, and is thought to be related to the SFE of the material [14]. It is generally accepted that FCC metals and alloys with a SFE lower than 18 mJ/m^2, and higher than 22 mJ/m^2 exhibit TRIP and TWIP effects, respectively [15,16]. In a previous study, it has been shown that the SFE of LPBFed 316L SS with various process parameters is about 14 ± 5 mJ/m^2 [11], which makes this alloy prone to strain-induced martensitic transformation during room temperature deformation. However, reports show that, in contrast with its wrought

* Corresponding authors.
E-mail addresses: fuhanwei@buaa.edu.cn (H. Fu), p.rivera1@lancaster.ac.uk (P.E.J. Rivera-Díaz-del-Castillo).

https://doi.org/10.1016/j.msea.2022.143882
Received 19 July 2022; Received in revised form 24 August 2022; Accepted 24 August 2022
Available online 29 August 2022

counterparts, LPBF processing can suppress TRIP effect in 316L SS due to increased austenite stability as a result of thermal cycling [17].

The origin of high ductility in LPBFed 316L SS has been discussed in previous reports. There is enough evidence that deformation twinning and dislocation slip are activated during deformation [18–22]. It has also been reported that TWIP is the main reason for the high ductility of such material. Some studies revealed that the interactions between twins and the cellular structures formed during LPBF due to rapid solidification control strain hardening [23]. Wang et al. [8] indicated that solute segregation along the cell walls and low-angle grain boundaries (LAGBs) can enhance dislocation pinning and promote the formation of twins during straining. The presence of deformation-induced DRX grains is also reported in a handful of previous studies [10,11]. Lattice rotation and a gradual increase in the misorientation of LAGBs and their transformation into HAGBs, as well as a deformation twinning-induced DRX mechanism are suggested for the formation of DRX grains during tensile testing at room temperature in LPBFed 316L SS [10,11]. However, the role of DRX in the improvement or deterioration of strain hardening has not been explored yet. To the best of the authors' knowledge, no strain hardening model incorporating DRX has been reported for LPBFed 316L SS.

Depending on the dislocation types, various strain hardening mechanisms can be activated during straining. Dislocation arrays can be categorised into statistically stored dislocations (SSDs), and geometrically necessary dislocations (GNDs) [24]. SSDs are the result of the random trapping of dislocations in the bulk; their accumulation usually leads to forest hardening [25]. GNDs are formed due to geometrical constraints of the crystal lattice such as grain/subgrain boundaries, dislocation cell walls, and twin boundaries; their pile up leads to the development of a back-stress [25]. Although their investigation results in a deeper understanding of their deformation mechanisms, such studies have not been done yet for LPBFed alloys. The characterisation of SSDs is difficult, because they have a net zero Burgers vector, but GNDs can be characterised and quantified by electron backscatter diffraction (EBSD) with a resolution in the range of 0.1°–0.2° and step sizes of 0.5–1 μm [26]. Since reaching a resolution of 0.1°–0.2° is hardly attainable, the cross-correlation EBSD method is suggested by Jiang et al. [27] for a more precise estimation of the GND density.

The objective of this work is to introduce a unified modelling approach to describe quantitatively the strain hardening mechanisms and microstructural evolution in LPBFed 316L SS. This model incorporates dislocation hardening, the dynamic Hall–Petch effect (introducing twin obstacles), and DRX. The storage of GNDs and SSDs, their evolution, and their role in strain hardening is investigated.

2. Experimental procedure

316L SS flat tensile testing samples were built in an argon environment (to avoid oxidation) by LPBF using a Renishaw plc AM125 machine, with the tensile axis at a 5° angle from the build direction to ensure the optimised application of the support structures, in order to minimise distortion after removing the parts from the supports; the detailed processing parameters and sample geometry were described in a previous study [28]. Gas atomised 316L SS powder with a particle size distribution of 15–45 μm and a mean value of around 30 μm was used as feedstock (Fig. 1a). The particles were spherical, with only a few satellites. Table 1 shows the chemical composition of the as-received powder. As shown in Fig. 1b, the samples for EBSD and transmission electron microscopy (TEM) characterisation prior to deformation were obtained from the grip of the as-printed tensile testing specimen (the area that had not been strained during tensile testing, blue rectangle). EBSD and TEM samples after failure were extracted from an area quite close to the fracture surface, as schematically shown in Fig. 1b (red rectangle).

Tensile testing was performed at room temperature at an initial strain rate of 10^{-4} s^{-1} using an Instron 3382 universal testing machine.

Table 1
Chemical composition of the powder in wt.%.

Fe	Cr	Ni	Mo	Mn	Si	P	S	N	C	Cu
Bal.	17.75	12.75	2.38	2	0.75	0.025	0.01	0.1	0.03	0.5

The reported strength and ductility values were the average of 3 tests. Scanning electron microscopy (SEM) observations were conducted in a Tescan Mira 3 LMHP field emission SEM to characterise the powder morphology. EBSD was employed to examine grain orientation, average local misorientation, grain boundary structure, and recrystallisation occurrence in a Tescan Mira 3 LMHP field emission SEM equipped with OXFORD instruments symmetry EBSD detector at a scanning step size of 0.8 μm and 0.5 μm prior to and after deformation, respectively. HKL Channel 5 data post-processing software was used to produce the related EBSD maps. A binning size of 8 × 8 was used to capture the maps, and 156 × 128 pixel patterns were collected. Noise reduction was conducted in the Channel 5 software at level 4. The grains were identified as high-angle grain boundaries (HAGBs) and the subgrains as LAGBs; their sizes were measured by the line intercept method using EBSD grain boundary maps. The grain boundaries were classified according to their misorientation angle into LAGBs ($2° \leq \theta < 15°$) and HAGBs ($\theta \geq 15°$). Kernel average misorientation (KAM) is defined as the average value of eight neighbouring misorientations between a kernel scanned point and its eight closest neighbouring scanned points. When calculating KAM, any nearby misorientation angles greater than 5° are disregarded.

TEM was used for further characterisation of nanometre scale features such as dislocations, dislocation cells, and deformation twins. Three-mm diameter disks were machined out of the samples, ground to 50 μm thickness, and thinned using Gatan 691 Ion Beam Thinner for TEM using TECNAI G20 at 200 kV.

3. Results

3.1. Mechanical properties

Fig. 2a shows the true stress–strain curve and the corresponding strain hardening rate of the LPBFed 316L SS. Table 2 lists the average values of the mechanical properties of LPBFed 316L SS. The strain hardening rate showed a constant reduction. To better understand the deformation mechanisms, the instant strain hardening exponent (n) was plotted as a function of true strain to analyse the strain hardening capability of the alloy (Fig. 2b). n is given by [29]:

$$n = d(\ln \sigma)/d(\ln \epsilon), \tag{1}$$

where σ is the true stress and ϵ is the true strain. Most metals and alloys have n values ranging between 0.1 to 0.5. In this study, the LPBFed 316L SS exhibits n values between 0.05 and 0.3. This n range is broader than that reported by Voisin et al. [30], 0.05–0.2 for the as-built LPBFed 316L SS. The n values of the present steel are similar to those reported for the LPBFed 316L SS after annealing at 1000 °C for 1 h in the same publication [30]. This shows that the strain hardening capability of the present steel is higher than the steel produced in [30], and it is closer to a LPBFed and recrystallised alloy. The alloy behaviour can be divided into three stages (Fig. 2b):

- Stage A: n decreases from infinity to ~0.05 at $\epsilon = 0.04$, then it rapidly increases to 0.15 with a sharp transition around $\epsilon = 0.1$.
- Stage B: n increases moderately to 0.2 up to $\epsilon = 0.22$.
- Stage C: A maximum rate of n growth peaking at $\epsilon = 0.27$, followed by n decline.

After $\epsilon = 0.27$, the deformation is non-uniform, and as a result of this, strain hardening mechanisms are not described for strains higher than 0.27 in this work. Abrupt changes in n values such as those

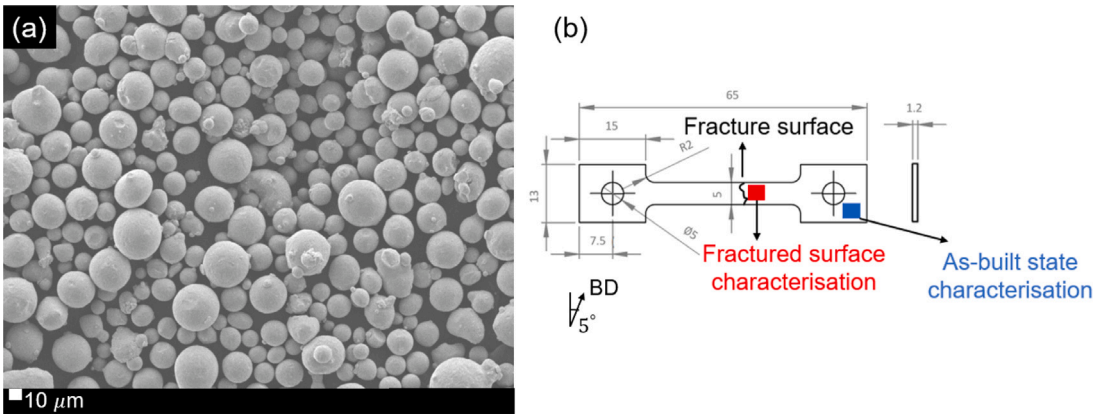

Fig. 1. (a) SEM images of the particle size distribution of as-received 316L powder. (b) Dimensions of the tensile testing specimen. Build direction (BD) is indicated. Characterisation samples are shown schematically in blue and red rectangles representing the as-built state and fractured state, respectively. (For interpretation of the references to colour in this figure legend, the reader is referred to the web version of this article.)

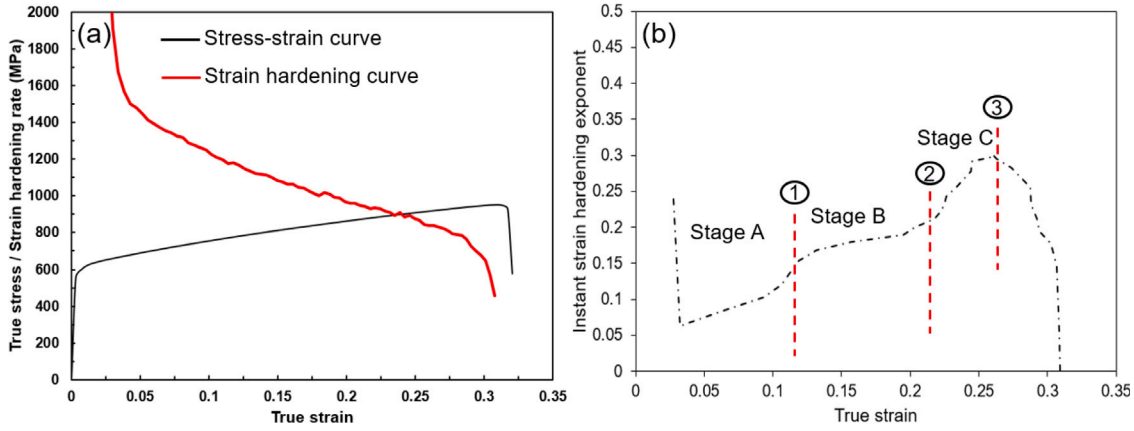

Fig. 2. (a) Tensile true stress–strain curve of the LPBFed 316L SS and the corresponding strain hardening curve. (b) Instant strain hardening exponent as a function of true strain, indicating the strain hardening capability of the LPBFed 316L SS.

Table 2
Mechanical properties values of LPBFed 316L SS.

True yield strength (MPa)	True ultimate tensile strength (MPa)	Fracture strain
600 ± 5	952 ± 7	0.32 ± 0.01

observed at ϵ = 0.1, 0.22, and 0.27 can be related to transitions of deformation mechanisms [30], and marked as 1, 2, and 3, respectively. Such transitions are highlighted in Fig. 2b by dashed lines.

3.2. Microstructure

Previous investigations of LPBFed 316L SS implementing several characterisation techniques including EBSD and TEM have revealed the most important aspects of the microstructure of this steel under deformation: grains/subgrains, mechanical twins, dislocation cells, and DRX [3,11,31]. Fig. 3 presents various microstructural features that can be identified by EBSD after fracture of the present LPBFed 316L SS. Fig. 3a shows a representative image quality (IQ) map of the fractured sample area (Fig. 1b, red) featured with deformation bands that can be seen in most grains. Fig. 3b shows the corresponding post-fracture inverse pole figure (IPF) map. HAGBs are indicated in black. The majority of the grains have orientations close to ⟨101⟩ and ⟨111⟩ parallel to the build direction, as indicated by the green- and blue-coloured grains in Fig. 3b. The variation of the texture in the present study was consistent with earlier reports on LPBFed 316L SS [32–34]. Deformation bands with two variants close to ⟨101⟩ and ⟨100⟩ directions can be recognised. Fig. 3c shows the twin boundary map of the fractured sample depicting that the characterised deformation bands in Fig. 3a and b are mechanical twins. As expected, the fractured material was characterised by large deformation twins. Deformation twins are mostly formed in grains with ⟨101⟩ and ⟨111⟩ directions, which is consistent with previous reports [3,34]. The volume fraction of twins based on several EBSD maps is estimated to be 0.28. Deformation twinning plays an important role in the ductility of materials with low SFE, as twin boundaries act as effective dislocation barriers during deformation. The twin-mediated reduction of dislocation mean free-path has been referred to as dynamic Hall–Petch effect, which promotes the strain hardenability and delays the onset of necking [35]. The distribution of LAGBs and HAGBs in the fractured state is shown in Fig. 3d, where statistical results show that 60% of the boundaries are high-angle. The distribution of LAGBs and HAGBs of the present steel in the as-built state was reported in a previous publication [6], and represented in the supplementary file (Fig. S1). An increased fraction of HAGBs after fracture from 30% in the LPBF as-built condition to 60% occurred, despite the fact that subgrains (grains with boundaries coloured in yellow) are refined significantly after fracture compared to the as-built state. In addition to a substantial refinement in subgrain size (comparing Fig. 3d and Fig. S1), the transformation of LAGBs to HAGBs can be recognised. Subgrain size refinement can be related to an increase in both dislocation density and dislocation slip due to plastic deformation. It can be claimed that an increase in the misorientation of LAGBs towards becoming HAGBs is related to the formation of deformation twins.

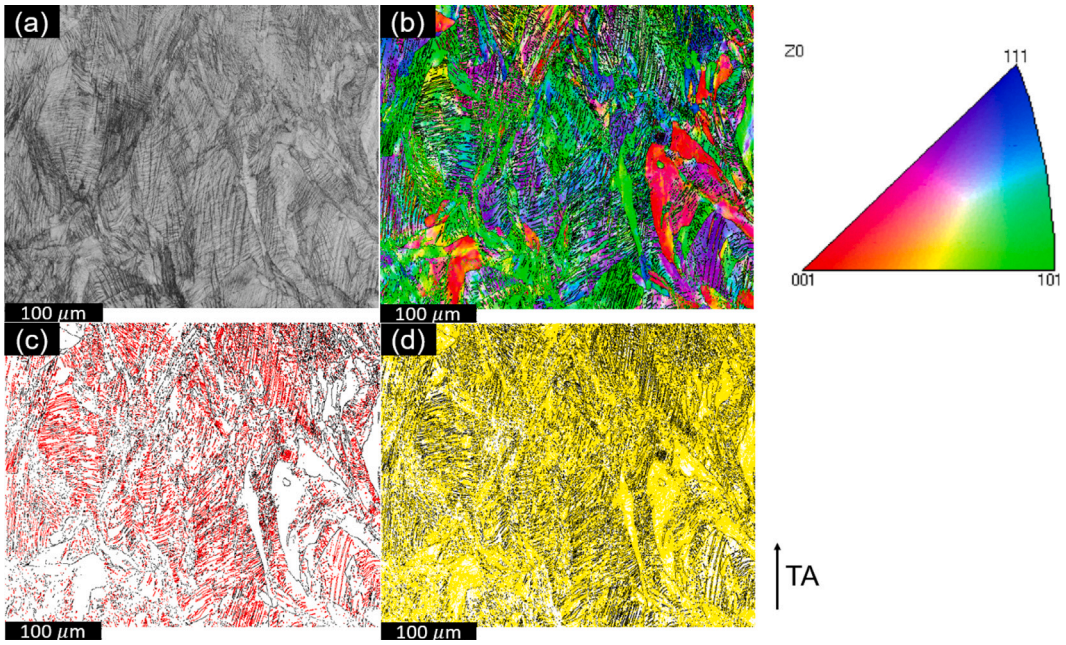

Fig. 3. (a) EBSD IQ map indicating the fractured microstructure containing several deformation bands. (b) EBSD IPF map showing grains orientation according to the plane parallel to the build direction. (c) EBSD twin boundary map showing the distribution of twins in red. (d) EBSD grain boundary map showing HAGBs and LAGBs in black and yellow, respectively. TA denotes tensile axis, which is parallel to the build direction. (For interpretation of the references to colour in this figure legend, the reader is referred to the web version of this article.)

The kernel average misorientation (KAM) maps (Fig. 4a and b) depict local changes in lattice orientations caused by lattice rotation or distortion. Such rotations/distortions stem from dislocations produced during tensile testing interacting with LPBF thermal and residual strains (Fig. 4a and b). As a result, the local variations in the KAM map can serve as a qualitative representation of both residual stress/strain and GND density. It should be noted that total dislocation density involves GNDs as well as SSDs. The as-built state showed little local misorientation, as evidenced by the dominance of the blue colour (Fig. 4a). Prior to deformation, a heterogeneous GND accumulation, with KAM values of about 2° in the LAGBs is observed (comparing Fig. 4a with Fig. S1), with limited misorientation within the grains/subgrains. Riabov et al. [31] demonstrated that strain accumulation occurs around cell boundaries in as-built and deformed LPBFed 316L SS samples. They used a finer EBSD scanning step size than the one used in this study to demonstrate the ability of dislocation cells to pin dislocations. Considering dislocation cell formation as a subprocess for the evolution of LAGBs [6], and that LAGBs can pin the dislocations [6], the current results confirm the importance of cell boundaries and LAGBs in LPBFed 316L SS plasticity.

In contrast with the as-built state, the fracture-surrounding areas had a very high local misorientation, due to straining, as well as areas that are strain-free, as denoted by blue colour (Fig. 4b). However, KAM maps cannot account for the elastic stresses in the material, and very high KAM values could also be related to very high elastic stress/strain accommodated in such regions [36]. Similar to what had been done in a previous study of the authors [11], to confirm the presence of partially/fully recrystallised areas, a recrystallisation map of the same area has been generated and shown in Fig. 4c. It can be seen that the areas characterised as strain-free (blue in Fig. 4b) correspond with those recrystallised (blue in Fig. 4c) or partially recrystallised/recovered (yellow in Fig. 4c). It should be noted that recrystallised, partially recrystallised/recovered, and deformed (red in Fig. 4c) regions are determined by EBSD post processing HKL Channel 5 software based on the internal average misorientation angle inside each grain. If the average misorientation angle within a grain exceeds a 2° threshold, the grain is defined as deformed. Grains with an average misorientation under 2°, but misorientation across subgrains above 2°, are partially recrystallised/recovered. The remaining grains i.e. those with average and local misorientations under 2° are categorised as recrystallised, in agreement with well-established literature [34,37–41]. DRX regions can be observed at the intersections of deformation twins by comparing Figs. 4c and 3c. For a better comparison, the highly populated twinned and recrystallised areas are highlighted with dashed rectangles in the supplementary file, Fig. S2. The occurrence of DRX during room temperature deformation of LPBFed 316L SS is consistent with the results of previous studies [10,12]. A thermostatistical model to estimate the critical strain for the activation of twinning-induced DRX is presented in [11]. Strain-free regions can also be observed in the TEM micrograph shown in Fig. 5. It must be noted that as the grain size (size of the grain with HAGBs) is measured as 35 ± 9 μm [6]; and the detecting of a whole recrystallised grain with TEM is quite challenging. Therefore, only EBSD has been used to characterise recrystallised/recovered grains in this study.

Fig. 6 presents TEM images showing grains exhibiting dislocation cells prior to and after deformation. In the as-built structure, dislocation cellular structures that are commonly observed in LPBFed alloys are present in Fig. 6a with an average size of 400 nm. Cell walls are observed to be decorated with a higher density of dislocations compared to their interiors. After deformation, three scenarios are observed for cellular structure evolution: (i) some cells are refined through the pile up of dislocations into their walls (Fig. 6b). (ii) some cells are cut by LAGBs (Fig. 6c) and (iii) deformation twins (Fig. 6d). It can be concluded that most of the existing cellular structures from the LPBF as-built state do not constitute strong barriers to dislocation motion, compared to LAGBs and deformation twins. However, their interactions with grains/subgrains and twin boundaries may influence the dislocation mean free path, and subsequently the strain hardening capability of the build.

Therefore, our approach to model strain hardening considers a combination of dislocation slip, deformation twinning, and DRX. Moreover, an analysis regarding the type of dislocations that evolve during deformation sheds light into the mechanisms governing strain hardening in LPBFed 316L SS.

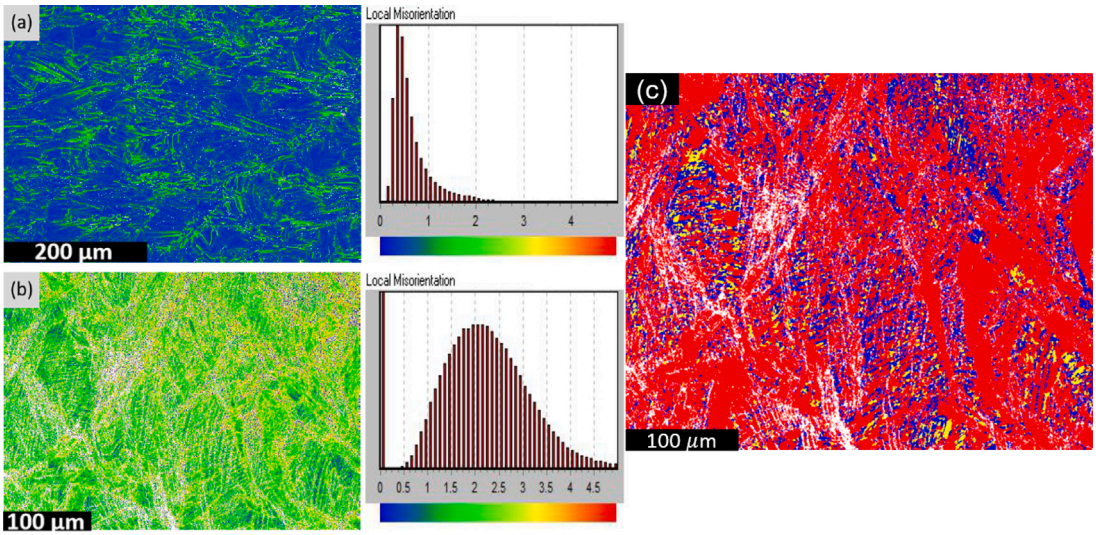

Fig. 4. (a) Representative EBSD KAM map of the as-built steel. (b) Representative EBSD KAM map of the fractured steel. (c) Representative EBSD recrystallised map, showing recrystallised, partially recrystallised/recovered, and deformed regions in blue, yellow, and red, respectively [11]. (For interpretation of the references to colour in this figure legend, the reader is referred to the web version of this article.)

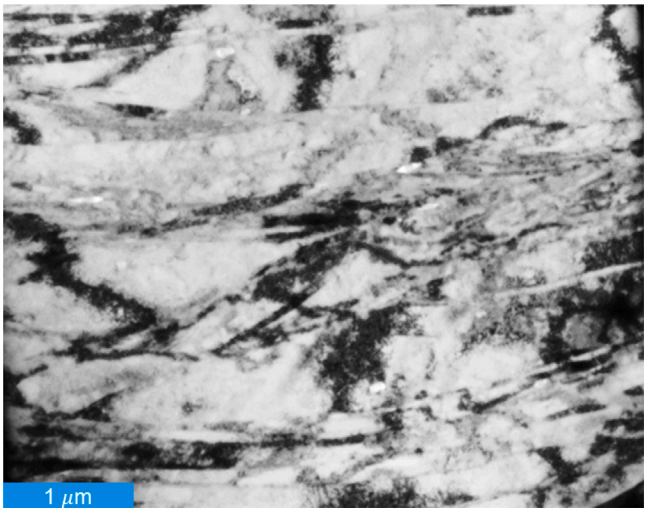

Fig. 5. (a) Representative bright field TEM micrograph showing strain-free regions (white regions) in the fractured LPBFed 316L SS.

4. Modelling

4.1. Flow stress modelling

The evolution of dislocation density where deformation twinning is present can be described using a rule of mixtures incorporating both contributions [42]:

$$d\epsilon = (1 - f_{tw})d\epsilon_{dis} + \epsilon_{tw}df_{tw}, \tag{2}$$

where f_{tw} is the volume fraction of twins, $d\epsilon_{dis}$ is the increase in strain as a result of dislocation slip (on the untwinned area), ϵ_{tw} is the strain induced by the formation of twins, and df_{tw} is the increase in twin volume fraction. From Eq. (2), the variation of dislocation slip with strain $\frac{d\epsilon_{dis}}{d\epsilon}$ can be described as:

$$\frac{d\epsilon_{dis}}{d\epsilon} = \frac{1}{1 - f_{tw}}\left(1 - \epsilon_{tw}\frac{df_{tw}}{d\epsilon}\right). \tag{3}$$

It is well-established that the most active twinning system in FCC metals is $\{111\}\langle 112\rangle$ [43]. The shear strain for twinning on this system is $\gamma_{tw} = \frac{\sqrt{2}}{2}$. Shear strain is related to the normal strain through the Taylor factor (M): $\epsilon = \gamma/M$. Therefore, Eq. (3) can be rewritten as:

$$\frac{d\epsilon_{dis}}{d\epsilon} = \frac{1}{1 - f_{tw}}\left(1 - \frac{\sqrt{2}}{2M}\frac{df_{tw}}{d\epsilon}\right). \tag{4}$$

Dislocation density ρ evolution as a function of true strain can be expressed as:

$$\frac{d\rho}{d\epsilon} = \frac{d\rho}{d\epsilon_{dis}}\frac{d\epsilon_{dis}}{d\epsilon} = \frac{d\rho}{d\epsilon_{dis}}\frac{1}{1 - f_{tw}}\left(1 - \frac{\sqrt{2}}{2M}\frac{df_{tw}}{d\epsilon}\right). \tag{5}$$

According to Kocks–Mecking theory for strain hardening, $d\rho/d\epsilon_{dis}$ is a result of the competition between dislocation storage and annihilation due to dynamic recovery and/or recrystallisation [44]. Dislocation storage strongly depends on the dislocation mean free path Λ, which is limited by the dislocation forest, grain boundaries, and twin boundaries. Previous studies on the strengthening mechanisms in LPBFed alloys show that subgrain boundaries prevail as barriers to dislocation motion compared to conventional grain boundaries [6,30]. Thus, in this approach, subgrain size D_s is chosen as the dislocation impedance feature. Λ can be expressed as:

$$\frac{1}{\Lambda} = k_1\sqrt{\rho} + \frac{1}{D_s} + \frac{1}{L}, \tag{6}$$

where $k_1 = \frac{1}{30}(\frac{\mu}{\mu_0})^2$ is the dislocation storage coefficient, μ is the shear modulus, μ_0 is the shear modulus at 0 K, and $\frac{1}{L}$ represents the inverse intertwin spacing, the average reduction in dislocation mean free path caused by twin formation and growth [42]:

$$\frac{1}{L} = \frac{1}{2e}\frac{f_{tw}}{1 - f_{tw}}, \tag{7}$$

where e is the average twin thickness. The dislocation storage rate $d\rho^+/d\epsilon_{dis} = M/b\Lambda$, where b is the magnitude of the Burgers vector. Therefore the evolution of dislocation density as a result of dislocation slip is expressed as:

$$\frac{d\rho}{d\epsilon_{dis}} = \frac{d\rho^+}{d\epsilon_{dis}} - \frac{d\rho^-}{d\epsilon_{dis}} = M\left(\frac{k_1}{b}\sqrt{\rho} + \frac{1}{bD_s} + \frac{1}{2eb}\frac{f_{tw}}{1 - f_{tw}} - (f_{DRV} + f_{DRX})\rho\right), \tag{8}$$

where f_{DRV} and f_{DRX} are the dynamic recovery (DRV) and dynamic recrystallisation coefficients, respectively. The term $(f_{DRV} + f_{DRX})\rho$ accounts for the overall dislocation annihilation $d\rho^-/d\epsilon_{dis}$. DRX is the subsequent annihilation process that decreases the dislocation density

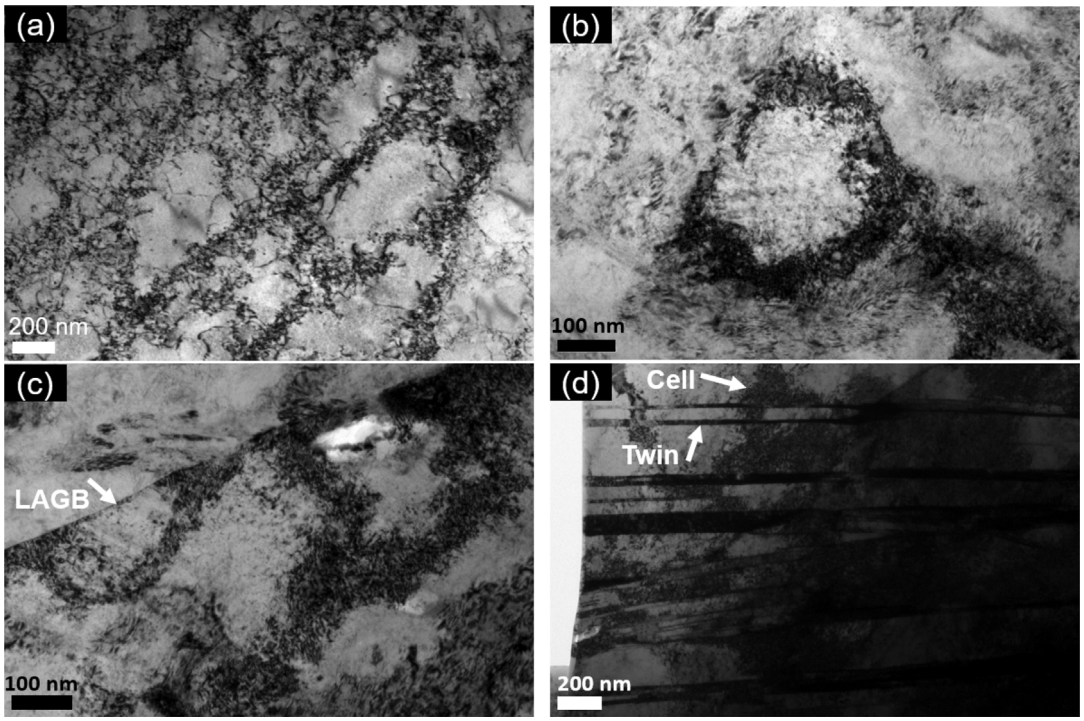

Fig. 6. Representative bright field TEM images showing (a) the presence of dislocation cells prior to deformation, (b) a dislocation cell after fracture, (c) the dislocation cells that can be cut by LAGBs during deformation, and (d) the growth of deformation twins through the dislocation cells during deformation.

since dislocation-free grains nucleate and grow from highly dislocated subgrains and/or deformation twins [45]. In order to solve Eq. (8), the volume fraction of twins and their evolution as a function of strain should be estimated. According to Bouaziz et al. [46] the twin fraction is related to the strain via:

$$f_{tw} = F_0\left(1 - \exp[-\beta_0(\epsilon - \epsilon_{tw})]\right)^m, \tag{9}$$

where F_0 is the maximum twin fraction, β_0 is the twinning kinetic parameter, ϵ_{tw} is the critical strain for the onset of twinning, and m is a constant. By differentiating Eq. (9) with respect to strain, the evolution of twin fraction with strain is expressed as:

$$\frac{df_{tw}}{d\epsilon} = F_0\beta_0 m \exp\left(-\beta_0(\epsilon - \epsilon_{tw})\right)\left[1 - \exp\left(-\beta_0(\epsilon - \epsilon_{tw})\right)\right]^{(m-1)}. \tag{10}$$

In addition to the contribution of dislocations to strain hardening, twins, cells, and grain boundaries also affect strain hardening, as their interactions with the matrix causes an overall back-stress, which value can be estimated via [47]:

$$\sigma_T = M\mu b\beta\left(\frac{1}{L} + \frac{1}{D_s} + \frac{1}{d_c}\right), \tag{11}$$

where d_c is the dislocation cell size and β is a geometric constant. The term $(1/L + 1/D_s + 1/d_c)$ accounts for dislocation pile-ups at twins, subgrain boundaries, and cell walls, respectively.

Therefore, the flow stress σ_{flow} of the LPBFed 316L SS can be described as:

$$\sigma_{flow} = \sigma_Y + \sigma_D + \sigma_T = \sigma_Y + \alpha M\mu b\sqrt{\rho} + M\mu b\beta\left(\frac{1}{L} + \frac{1}{D_s} + \frac{1}{d_c}\right), \tag{12}$$

where σ_Y is the yield strength, σ_D is the dislocation forest hardening (Taylor's relationship [44]), and σ_T is the back-stress hardening caused by deformation twin interactions with interfaces. It should be noted that the dislocation forest hardening contributes to the yield strength. After the beginning of the plastic deformation, the newly generated dislocations multiply and will be added to the dislocations stored in the material prior to plastic deformation, increasing the flow stress. The modelling approach presented here is the first to simultaneously combine dislocation generation, recovery, twinning, and recrystallisation.

4.2. Dislocation type

Two methods are used to estimate the GND density of the present steel. Prior to deformation, EBSD KAM map is used to measure GND density [36]:

$$\rho_{GND} = \frac{\alpha\theta}{bx}, \tag{13}$$

where $\alpha = 2$ is a constant, θ is the KAM angle in radians, and x is the EBSD step size. In order to model the evolution of ρ_{GND} with strain, the Ashby's model has been used [25]:

$$\rho_{GND} = \frac{\epsilon}{4b}\left(\frac{1}{D_s} + \frac{1}{2e}\frac{f_{tw}}{1 - f_{tw}} + \frac{1}{d_c}\right). \tag{14}$$

The term in brackets considers the same dislocation mean free path that has been used to describe the contribution of twinning in strain hardening, as the importance of the subgrain boundaries and dislocation cell walls in trapping dislocations are well-established in previous studies. Since the total dislocation density (ρ) can be estimated from the Taylor's relationship [44] (σ_D term, which is the second strengthening term in Eq. (12)), the SSD density can be approximated by:

$$\rho_{SSD} = \rho - \rho_{GND}. \tag{15}$$

5. Analysis

5.1. Twinning and development of back-stress

The critical resolved normal stress (σ_T^{crit}) for twin nucleation during deformation can be calculated as [48]:

$$\sigma_T^{crit} = \frac{6 \times SFE}{b_p}, \tag{16}$$

Table 3
Numerical values of the physical parameters and constants used in various formulations in this work.

Parameter	Value	Source
F_0	0.28	EBSD analysis
m	2	[49]
e (nm)	150	TEM and EBSD analysis
μ (Pa)	$(88\,884.6\text{-}37.3T) \times 10^6$	[52]
M	3.06	[44]
b (nm)	0.25	[44]
β	0.24	[47]
β_0	20	Fitted to experiment
V (m^3/mol)	39×10^{-23}	Present work
E (Pa)	210×10^9	[53]
ϵ_p	0.14	[28]
ν	0.3	[54]
c (m/s)	5280	[55]
D_s (μm)	10	[6]
d_c (nm)	400	TEM analysis
N_A (atoms)	6.02×10^{23}	–
ρ_a (kg/m^3)	8000	[56]
w_a (g/mol)	55.84	Present work
$f_{DRV}+f_{DRX}$	Various	Fitted to experiment

where $SFE = 14$ mJ/m^2 is the SFE of the present steel [11] (measured from TEM observations), and $b_p = 0.14$ nm [48] is the magnitude of the Burgers vector of the twin source. Therefore, $\sigma_T^{crit} = 600$ MPa. This shows that TWIP effect begins at the onset of plastic deformation in the LPBFed 316L SS (Table 2). Using Eq. (9), Fig. 7a shows the evolution of twin volume fraction during tensile deformation. Quantitative measurements from EBSD showed that the twin volume fraction after fracture is 0.28 (Fig. 3c); this value has been considered as F_0. The physical parameters used for solving the mathematical formulations in this work are listed in Table 3. All the parameters that are presented in Table 3 are calculated from EBSD and TEM analysis implemented in this work, or have been taken from similar previous works in the literature, except from β_0, which is fitted to experimental results in this work. Knowing the final value of the f_{tw} from EBSD analysis, $\beta_0 = 20$ is fitted to experimental results. This value is significantly larger than that of reported for wrought 304L SS [49] and Fe-22Mn-0.6C TWIP steel [50] (1.35 and 3, respectively); however, it is similar to wrought Fe-18Mn-0.6C TWIP steel with and without the addition of Al ($\beta_0 = 14$–26) and a very fine average grain size (4 μm) [51]. The average twin thickness e is taken as 150 nm. Both micro-twins in Fig. 3c and nano-twins, for which representative TEM images are shown in Fig. 8, are considered to estimate e. The twin volume fraction increased from the onset of plastic deformation from 0 to ~28%, whereas the intertwin spacing (L) decreased gradually during deformation (Fig. 7b) from 2.1 μm to 770 nm. Thus, the contribution of deformation twins during deformation is plotted in Fig. 7c. It follows that the direct contribution of deformation twins into flow stress is not very significant. σ_T approaches a plateau at a strain of 0.1, which is detected as the end of Stage A with a sharp increase of the instant strain hardening exponent (strain hardening capability) (Fig. 2b).

5.2. Overall dislocation density progress

The evolution of total dislocation density during tensile deformation is modelled and plotted in Fig. 9a, where it raised from an initial value of 7.8×10^{14} m^{-2} to 1.1×10^{15} m^{-2} at the ultimate tensile stress. The evolution of restoration mechanisms (DRV and DRX) coefficient, which is the representative of the softening ability of the alloy during deformation, is fitted to experimental results and shown in Fig. 9b. In addition to β_0, the only parameter fitted in this work is $f_{DRV} + f_{DRX}$, which is significantly increased from an initial value of 0 at the beginning of deformation to 9 at a strain of 0.15, then it gradually decreased to a value of 7.7 at a strain of 0.31, and finally it increased abruptly to 14 until a strain of 0.33. Based on a previous study by the authors, the critical strain to activate DRX at room temperature for the present steel is 0.23 [11]. This indicates that the annihilation processes are mainly controlled by dynamic recovery at the two first stages of strain hardening, and by DRX thereon.

Table 4
Evolution of the number of impingement dislocations with f_{DRV}.

N_d	f_{DRV}	Point in Fig. 9b
1	1	A1
4	2.9	A2
7	4.8	A3
10	7.3	A4
13	9.2	A5

To validate the fitted values for $f_{DRV}+f_{DRX}$, the f_{DRV} evolution is computed using the thermostatistical theory of plastic deformation [57]. In order to apply this approach to AM some modifications are made. According to Galindo-Nava et al. [58], the annihilation energy barrier G for a system consists of a term for the formation of dislocations U_{form}, a term for dislocation migration U_{mig}, which initiates dislocation glide towards annihilation, and a term for entropy, which is related to the degree of dislocation disorder as a function of temperature. Due to the very high residual stress that is already stored in LPBFed alloys, a stored strain energy term U_d must also be added to reduce the energy barrier for annihilation during deformation. This term can be estimated as [59]:

$$U_d = \frac{1}{2} V E \epsilon_p^2, \tag{17}$$

where V is the volume of a mole of the system (FCC structure), E is the elastic modulus, and ϵ_p^2 is the residual strain (plastic strain) stored in the alloy after LPBF.

The annihilation energy barrier G in LPBFed alloys can be expressed as:

$$G = U_{form} + U_{mig} - TS - U_d = \frac{1}{2}\mu b^2 l + \sigma_Y A_{act} b^2 l - TS - \frac{1}{2} V E \epsilon_p^2, \tag{18}$$

where l is the length of a dislocation segment that undergoes annihilation in a given volume under an applied stress, $A_{act} = \frac{\mu_0 l^* (2+\nu)}{12\pi(1-\nu)SFE}$ [45] is the activation area for annihilation, $l^* = 12.5b$ is the dislocation's distortion field length, ν is the Poisson's ratio, and $S = k_B \ln(\frac{\dot{\epsilon_0}}{\dot{\epsilon}})^N$ is the dislocation entropy. $\dot{\epsilon_0} = b\rho c$ is a maximum strain rate, where c is the speed of sound in the alloy, $\dot{\epsilon}$ is the deformation strain rate, and N is the dislocation's impingement effect, which accounts for the increase in microstates when the dislocations' strain fields overlap. $N = 1 + \frac{1}{3}(N_d - 1)$, where N_d is the number of dislocations impinging with the reference dislocation. When $N_d < 1$, N is considered to be 1. Following the mathematical expressions that were published in [58], f_{DRV} for an LPBFed FCC alloy takes the following form:

$$f_{DRV} = \frac{N_A \rho_a b^2 l^*}{w_a} \frac{k_B T \ln(\frac{\dot{\epsilon_0}}{\dot{\epsilon}})^N}{\frac{1}{2}\mu b^3 + \sigma_Y A_{act} b^3 - k_B T \ln(\frac{\dot{\epsilon_0}}{\dot{\epsilon}})^N - \frac{1}{2} V E \epsilon_p^2}, \tag{19}$$

where N_A is the Avogadro's number, ρ_a is the density of the bulk alloy, and w_a is the material's atomic weight. In the absence of impingement ($N = 1$), $f_{DRV} = 1$, which describes the experimental values at the beginning of plastic deformation (Fig. 9b). f_{DRV} raises with an increase in strain due to dislocation impingement. When the number of impinging dislocations (N_d) increases from 1 to 4, 7, 10, and 13, f_{DRV} values of 1, 2.9, 4.8, 7.3, and 9.2 are obtained, respectively (Table 4). This shows that, in contrast with their wrought counterparts, FCC LPBFed alloys have a pronounced tendency for dislocation annihilation due to higher impingement probability; this stems from a lower distance between dislocations in their as-built structures due to the presence of a residual stress.

The rate of dislocation multiplication/annihilation as a function of strain (using Eq. (8)) is also plotted in Fig. 9c. It shows an increasing rate from the onset of plastic deformation until a strain of about 0.2,

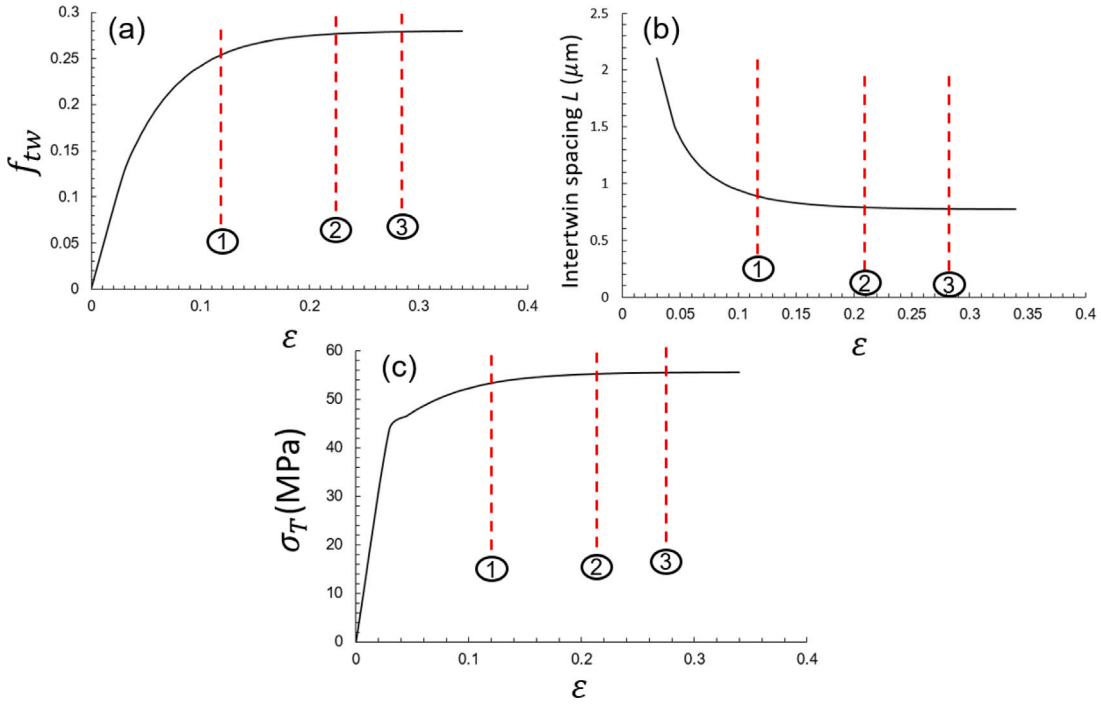

Fig. 7. (a) Evolution of twin volume fraction f_{tw} with strain. (b) Reduction in intertwin spacing L during straining due to formation of more twin obstacles. (c) Contribution of deformation twins in flow stress σ_T during deformation. Strain hardening capability stages are distinguished with red dashed lines.

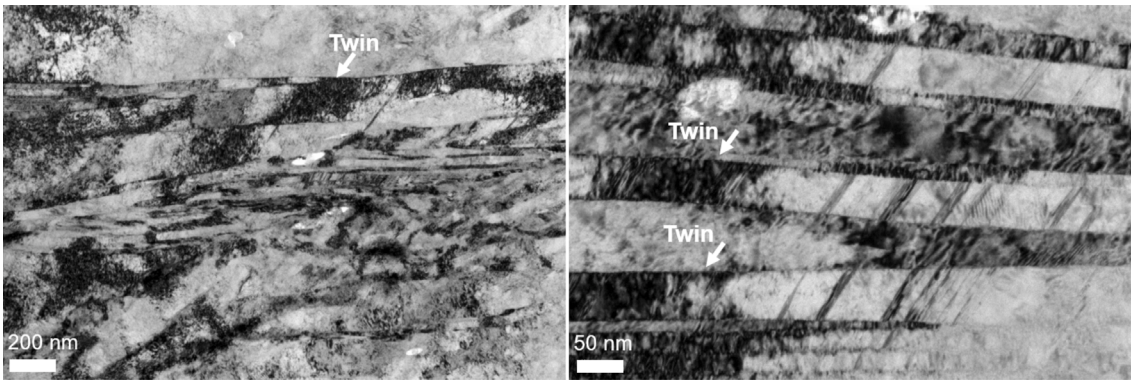

Fig. 8. Representative bright field TEM images showing twin thickness.

where it begins to become stabilised towards the end of deformation. Finally, the contribution of dislocations (σ_D) to the flow stress is shown in Fig. 9d, which increases almost linearly towards the ultimate tensile stress.

5.3. Forest vs. twin hardening

To better compare the contribution of dislocation and twin hardening to the flow stress, the difference between the instantaneous flow stress and the yield stress at different strains is plotted in Fig. 10a. At the onset of deformation, twinning dominates the strain hardening until a strain of 0.06. Afterwards, dislocation hardening dominates the total strain hardening mechanisms until fracture. The true stress–true strain curve of the LPBFed 316L SS is plotted again in Fig. 10b to show the contribution of various mechanisms into flow stress. The initial yield stress is 600 MPa, which is considered as a summation of the friction stress and the pre-existing dislocation forest.

5.4. Statistically stored vs. geometrically necessary dislocations

Fig. 11 shows the evolution of total dislocation density, as well as the density of GNDs and SSDs. The average GND and SSD densities are estimated from equations 14 and 15, respectively. Fig. 11 indicates that SSD density varies from 7×10^{14} m^{-2}, which is the major contributor to the total dislocation density at the beginning of deformation, to 6.5×10^{13} m^{-2}, at the failure strain. The average value of the GND density increases from 8×10^{13} m^{-2}, in the LPBF as-built state, to 8.8×10^{14} m^{-2}, after fracture. The majority of the total dislocations are SSDs before a true strain of ~0.17, and thereafter the GND density exceeds that of SSDs. For comparison, the measured total dislocation density, GND and SSD densities in a wrought high Mn TWIP steel during tensile deformation taken from [47] is also plotted in Fig. 11. At the beginning of deformation (at around a strain of 0.06), the LPBF total and SSD density are higher than that in wrought TWIP steel, but the GND density is similar for both steels. In contrast to TWIP steel, the SSD density in LPBFed steel decreases constantly until the end of deformation. The trend of GND variations for both steels is ascending, with the LPBFed steel growing with slightly higher values compared

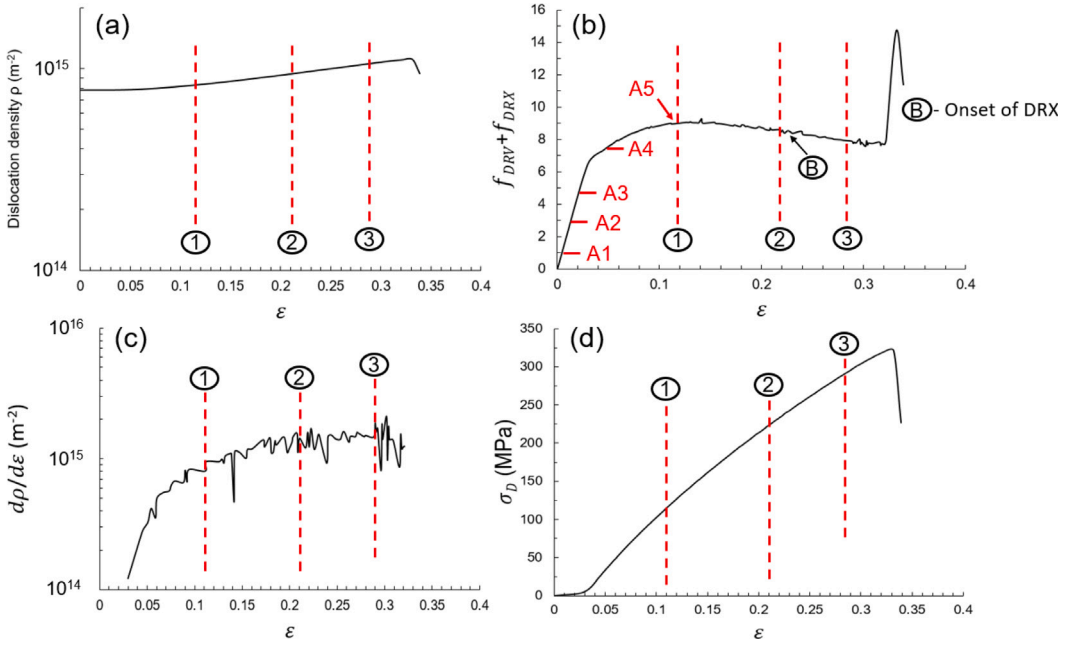

Fig. 9. Evolution of (a) total dislocation density ρ, (b) DRV and DRX coefficient, (c) rate of dislocation accumulation/annihilation, and (d) contribution of dislocation hardening during deformation. Strain hardening capability stages are distinguished with red dashed lines.

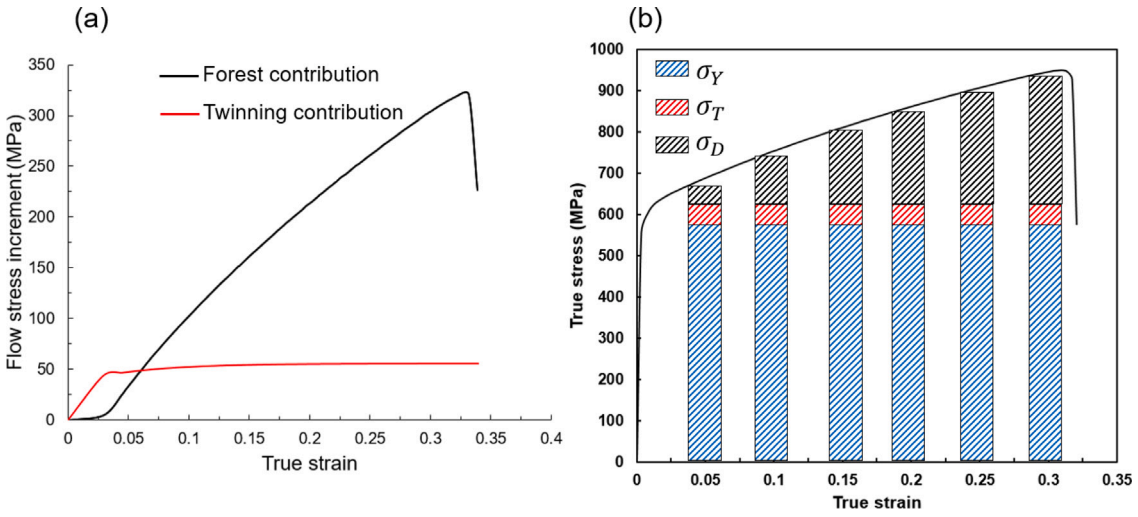

Fig. 10. Contribution of dislocation (σ_D) and twinning hardening (σ_T) to the stress increment during straining. σ_Y stands for yields stress.

to the TWIP steel. The most significant difference of the two steels derives from total dislocation density, which growth is very slow for the LPBFed steel, while the total dislocation density of the TWIP steel is at least three times higher than the LPBFed steel after a strain of 0.33. It can be concluded that strain hardening mechanisms in LPBFed and wrought TWIP steels are fundamentally different, and annihilation processes are more active in the LPBFed alloys.

In addition to a wrought TWIP steel, the dislocation types in LPBFed as-built structure of the present steel are compared to another 316L SS produced with another set of LPBF processing parameters [5], and to a LPBFed FeCoCrNi high-entropy alloy (HEA) [60] in Table 5. It can be seen that the densities of GNDs and SSDs are very similar in the two 316L SSs processed with different processing parameters. The HEA exhibits the same trend in the dislocation types with SSD density dominating the GND density in the as-built state. It is worth noting that the total dislocation density is measured using the Taylor's relationship. This shows the consistency of the results of the present work with previous reports on similar low SFE FCC alloys (see Table 5).

Table 5
Comparison of the density of different dislocation types in as-built LPBF state in other publications with the present study.

Alloy	ρ_{GND} (m^{-2})	ρ_{SSD} (m^{-2})	ρ (m^{-2})	Source
316L SS	9.84×10^{13}	6.81×10^{14}	7.84×10^{14}	[5]
FeCoCrNi HEA	1.53×10^{14}	5.02×10^{14}	6.55×10^{14}	[60]
316L SS	8×10^{13}	7×10^{14}	7.84×10^{14}	Present work

The uncertainty (error) of the GND density (ρ_{noise}) measurement via EBSD can be calculated from [47]:

$$\rho_{noise} = \frac{\delta}{bx}, \tag{20}$$

where δ is the angular resolution of the EBSD. Since for the present study an angular resolution lower than 0.05° (8.8×10^{-4} rad) could be obtained, an upper bound of 0.05° has been used to estimate the uncertainty. Therefore, the error of the GND density measurement by EBSD was 6.9×10^{12} m^{-2} and 4.4×10^{12} m^{-2} for step sizes of 0.5 and

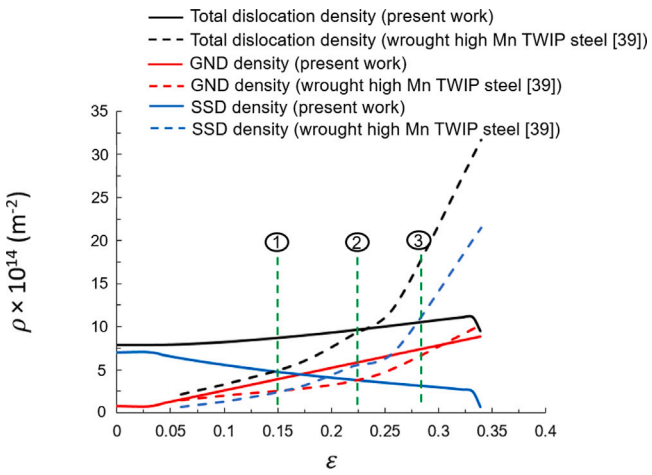

Fig. 11. Estimated total dislocation density from Taylor's hardening model, measured GND density, and estimated SSD density. Density of total, GNDs and SSDs during deformation of a wrought high Mn TWIP steel is also plotted for comparison [47].

0.8 μm, respectively. Since the initial GND density is estimated to be 8×10^{13} m^{-2} and it increased during straining, the error is significantly lower than the measured dislocation densities, which further confirms the reliability of our modelling approach.

6. Discussion

An integral modelling approach is presented to describe the microstructural evolution and strain hardening of LPBFed 316L SS. The model incorporates two important contributions: dislocations and twins. The initial dislocation density after LPBF, subgrain size, and dislocation cell size are input to calculate dislocation forest hardening and TWIP effect. The initial dislocation density, which is estimated from Taylor's relationship, is used for modelling dislocation multiplication/annihilation. The evolution of dislocation density is a competing process between (i) dislocation generation, as a result of dislocation interactions ($k_1\sqrt{\rho}$), as well as strain hardening caused by barriers to dislocation motion such as subgrain boundaries ($1/D_s$) and twin boundaries ($(1/2e)(f_{tw}/1-f_{tw})$), and (ii) dislocation annihilation processes, DRV and DRX. The annihilation processes are governed by DRV at the beginning and intermediate stages of deformation, and by DRX at the end of deformation; microstructural characterisation proves the dominance of DRX over DRV in the as-fractured state (Fig. 4c). Therefore, it can be considered that $f_{DRV} + f_{DRX} \simeq f_{DRV}$ for stages A and B, but $f_{DRV} + f_{DRX} \simeq f_{DRX}$ at stage C for the present steel.

6.1. Twinning and GNDs

The twinning kinetics, captured by $df_{tw}/d\epsilon$, is a key parameter in the present model as it influences both the dislocation contribution through the evolution of GNDs and the TWIP effect. $df_{tw}/d\epsilon$ is sensitive to the austenite stability, which depends on the SFE and the twinning kinetics parameter, β_0. An increase in SFE values of FCC alloys lead to a decrease in β_0, which can affect other parameters such as the maximum twin fraction, F_0, and even f_{DRV} and f_{DRX}. The β_0 adopted for the present steel is 20, which is close to the value of 26 for Fe-18Mn-0.6C TWIP steel reported by Jung and De Cooman [51], with a SFE of around 12 mJ/m^2. The SFE of the present steel is measured by direct TEM observations to be 14 mJ/m^2 [11]. The higher SFE of the present steel (compared to the high Mn TWIP steel) would demand a lower β_0 value; this is related to a higher austenite stability of the present steel compared to the mentioned high Mn TWIP steel. Another factor that can influence twinning kinetics is the strain rate, which is low enough in this study to provide enough time for twins to nucleate and grow. As it can be seen in Fig. 11, the GND density grows significantly during deformation due to a rapidly reduced dislocation mean free path caused by twin formation. Simultaneously, the SSD density reduced significantly during deformation due to the high DRV and DRX coefficient of the present alloy, increasing the strain hardenability of the material during straining. This is in contrast with wrought TWIP steels, where the GND and SSD densities grow simultaneously during tensile deformation [47]. This can be related to the very low annihilation rates of the conventionally processed alloys compared to LPBFed alloys.

6.2. Dislocation annihilation and impingement

In order to interpret the higher tendency of the LPBFed alloy for dislocation annihilation during room temperature deformation, an expression for f_{DRV} (Eq. (19)) is derived to account for the influence of a unique feature of LPBFed alloys on DRV coefficient, the residual stress. Interestingly, it has been shown that the number of impinging dislocations for LPBFed alloy increased with an increase in strain, which results in a higher ability for annihilation at room temperature. As the main mechanism for dislocation annihilation at room temperature is cross-slip, the distance between partial dislocations, which is controlled by SFE, plays an important role. In wrought alloys, the distance between dislocations is large, which means that dislocation impingement has a negligible effect, leading to a very low value of f_{DRV} during room temperature deformation. However, a high residual stress in LPBF as-built state enables dislocation multiplication, which subsequently increases the dislocation strain field impingement. This shows the importance of dislocation impingement caused by residual stress that is unique to LPBF on strain hardenability of such alloys. In the presence of such high residual stress, the distance between dislocations significantly reduces, making the alloy more prone to annihilation processes, which maintains the ductility of the alloy and prevents the microstructure to be saturated with both GND and SSD types, leading to a similar ductility to wrought alloys. Therefore, in LPBFed alloys, the decrease in SSD density during deformation is the key reason for high ductility.

Because of the importance of dislocation cells in yield strengthening of LPBFed 316L SS, their role in strain hardening should also be examined. As shown in Fig. 6b, dislocations can pile up at existing cell walls during deformation, further refining them to decrease strain energy. The evolution of dislocation cell size with dislocation density can be described via [57]:

$$d_c = \frac{k_c}{\sqrt{\rho}}, \tag{21}$$

where $k_c = \frac{12\pi(1-\nu)}{2+\nu}\left(1 + \frac{T\Delta S}{\frac{1}{2}\mu b^3}\right)$. Based on Eq. (21), the d_c at the beginning and end of deformation is 491 nm and 413 nm, respectively, which shows a slight cell refinement during tensile deformation. This is consistent with the findings of Riabov et al. [31]. This moderate change in cell size cannot produce significant back-stress changes, thus the contribution of cell size refinement to strain hardening can be ignored during deformation of LPBFed 316L SS. Therefore, cellular structures only contribute in reducing the intertwin spacing via increasing the GND density through reduction in the dislocation mean free path during tensile deformation.

6.3. Strain hardening mechanisms

As is plotted in Fig. 2b, the strain hardening capability of the LPBFed 316L SS can be divided into three stages, which are related to the several microstructural evolution phenomena during straining. In Stage A (ϵ = 0.03–0.13), deformation twins form quickly, reducing the dislocation mean free path significantly (dynamic Hall–Petch effect). This leads to an increase in the contribution of both twinning and

dislocation slip via deformation twins at this stage. Moreover, f_{DRV} increases abruptly from 0 to 9.25 in Stage A of deformation (Fig. 9b). This shows that the rate of dislocation annihilation is also very high, which keeps the strain hardenability of the present steel at a low level ($0.07 < n < 0.16$) at Stage A. The formation of twins and heavy dislocation annihilation rate is accompanied by a growth in GND density, as well as a drop in SSD density, respectively. This also shows that strain hardening primarily originates from the effective accumulation of GNDs, which concentrate adjacent to high energy sites such as LAGBs, HAGBs, and dislocation cell walls. However, the accumulation of GNDs is slowed by a high rate of dislocation annihilation and a high dislocation mean free path at Stage A.

Further increasing the strain (Stage B) leads to a saturation in twin formation and dislocation mean free path (Fig. 6a and b). The direct contribution of deformation twins to the strain hardening behaviour is very limited and saturated until the end of deformation (around 50 MPa). Thus, at high strains, the strain hardening capability originates from the evolution of total dislocation density. As the dislocation mean free path is at its minimum value due to mechanical twinning during Stage B, the GND density increases constantly, and after a strain of 0.17, GNDs prevail over SSDs. As dislocation annihilation rate is still high in Stage B ($7.56 < f_{DRV} < 9.25$), the SSD density decreases constantly as well. However, due to a decrease in f_{DRV} values at this stage, the strain hardening capability (n) is higher compared to Stage A.

Finally, at Stage C, microstructural evolution is affected by the activation of DRX; the critical strain for the activation of DRX in the present steel at room temperature is calculated to be 0.23 [11]. DRX activation improved the strain hardening capability of the alloy at this stage, by increasing more HAGBs, which can contribute to the evolution of GND density, improving the ability of the alloy to be strain hardened.

7. Conclusions

A dislocation-based model for strain hardening in a LPBFed austenitic TWIP SS is presented. The model is based on the contribution of dislocation structures, and recrystallisation, as well as twins in strain hardening. Dislocation storage is promoted due to the presence of LAGBs and the formation of twins, which act as obstacles that reduce the dislocation mean free path. Dislocation annihilation follows DRV and DRX activation during room temperature deformation. The TWIP effect is modelled considering the effects of LAGBs, dislocation cells, and twin–twin interfaces. Moreover, the evolution of GNDs and SSDs during deformation revealed more detailed information about strain hardening mechanisms. The following conclusions are drawn from this study:

1 Strain hardening in LPBFed TWIP steels can be divided into three stages. The TWIP effect dominates the strain hardening in moderate strains ($\epsilon < 0.1$). Using as input a combination of TEM and EBSD, the evolution of twin volume fraction and dislocation mean free path is modelled. They reach their saturation levels in Stage A. Because of very high annihilation rate at this stage, the strain hardening capability is the lowest compared to the succeeding deformation stages.
2 Significant twin formation occurs during Stage A of deformation; this stems from a very high twinning kinetics parameter, β_0, comparable to high Mn TWIP steels with similar SFEs. This leads to increasing the GND density, which is in its minimum value before the onset of plastic deformation. High values of DRV coefficient are accompanied with a decrease in SSD density, which is characterised as the main dislocation type of the LPBFed as-built 316L SS.
3 As twin volume fraction is constant at moderate and high strain levels, the direct contribution of TWIP effect remains constant in Stages B and C of deformation ($\epsilon > 0.1$). However, twins contribute to strain hardening through increasing GND density, as a result of interacting with LAGBs, dislocation cells, and other twins. A drop in DRV coefficient leads to an increase in strain hardening capability values in Stage B. In this stage, GNDs dominate the microstructure of the present steel. The strain hardening in this stage is mainly derived by the total dislocation hardening.
4 DRX is activated at Stage C ($\epsilon = 0.23$), increasing the strain hardening capability via generating more HAGBs that can lead to more increase in GND density. Strain hardening in Stage C is mainly governed by GND hardening.
5 A thermostatistical formulation specific to LPBFed alloys is presented to account residual stress to estimate the rate of dislocation annihilation. During room temperature deformation, LPBFed alloys undergo more pronounced dislocation annihilation processes such as DRV and DRX compared to their wrought counterparts. This stems from increased dislocation impingement as a result of much smaller distances between partial dislocations.
6 The results of the present work strongly suggests that uniform elongation of the LPBFed alloys is controlled primarily by the rate of DRV, which depends strongly on the number of impinging dislocation strain field from the onset of deformation. This is a direct consequence of the residual stress accompanying the build process.

CRediT authorship contribution statement

Hossein Eskandari Sabzi: Conceptualization, Methodology, Experimental data interpretation, Writing – original draft. **Xiao-Hui Li:** TEM and EBSD characterisation. **Chi Zhang:** TEM and EBSD characterisation. **Hanwei Fu:** TEM and EBSD characterisation. **Pedro E.J. Rivera-Díaz-del-Castillo:** Conceptualization, Methodology, Supervision and administration, Writing – review & editing.

Declaration of competing interest

The authors declare that they have no known competing financial interests or personal relationships that could have appeared to influence the work reported in this paper.

Data availability

The authors do not have permission to share data.

Acknowledgments

This work was supported by the Royal Academy of Engineering, United Kingdom (RCSRF1718/5/32), and by EPSRC, United Kingdom via DARE grant (EP/L025213/1). HF acknowledges the support by National Natural Science Foundation of China (51971011).

Appendix A. Supplementary data

Supplementary material related to this article can be found online at https://doi.org/10.1016/j.msea.2022.143882.

References

[1] H. Beladi, I.B. Timokhina, Y. Estrin, J. Kim, B.C. De Cooman, S.K. Kim, Orientation dependence of twinning and strain hardening behaviour of a high manganese twinning induced plasticity steel with polycrystalline structure, Acta Mater. 59 (2011) 7787–7799.
[2] A. Vinogradov, A. Lazarev, M. Linderov, A. Weidner, H. Biermann, Kinetics of deformation processes in high-alloyed cast transformation-induced plasticity/twinning-induced plasticity steels determined by acoustic emission and scanning electron microscopy: Influence of austenite stability on deformation mechanisms, Acta Mater. 61 (2013) 2434–2449.

[3] X. Wang, J.A. Muniz-Lerma, M.A. Shandiz, O. Sanchez-Mata, M. Brochu, Crystallographic-orientation-dependent tensile behaviours of stainless steel 316 L fabricated by laser powder bed fusion, Mater. Sci. Eng. A 766 (2019) 138395.

[4] H. Eskandari Sabzi, P.E.J. Rivera-Díaz-del Castillo, Composition and process parameter dependence of yield strength in laser powder bed fusion alloys, Mater. Des. 195 (2020) 109024.

[5] J. Fu, Sh. Qu, J. Ding, X. Song, Xu, M.W. Fu, Comparison of the microstructure, mechanical properties and distortion of stainless steel 316 L fabricated by micro and conventional laser powder bed fusion, Addit. Manuf. (2021) 102067.

[6] H. Eskandari Sabzi, E. Hernandez-Nava, X. Li, H. Fu, D. San-Martín, P.E.J. Rivera-Díaz-del Castillo, Strengthening control in laser powder bed fusion of austenitic stainless steels via grain boundary engineering, Mater. Des. (2021) 110246.

[7] Sh. Afkhami, M. Dabiri, H. Piili, T. Björk, Effects of manufacturing parameters and mechanical post-processing on stainless steel 316 L processed by laser powder bed fusion, Mater. Sci. Eng. A 802 (2021) 140660.

[8] Y.M. Wang, T. Voisin, J.T. McKeown, J. Ye, N.P. Calta, Z. Li, Z. Zeng, Y. Zhang, W. Chen, T.T. Roehling, et al., Additively manufactured hierarchical stainless steels with high strength and ductility, Nature Mater. 17 (2018) 63–71.

[9] W. Chen, T. Voisin, Y. Zhang, J. Forien, C.M. Spadaccini, D.L. McDowell, T. Zhu, Y.M. Morris, Microscale residual stresses in additively manufactured stainless steel, Nature Commun. 10 (2019) 1–12.

[10] A. Heidarzadeh, J. Zavašnik, R. Shabadi, R.T. Mousavian, Dynamic recrystallization's role in strength-ductility trade-off in polycrystalline Fe–Cr–Ni stainless steels produced by laser powder bed fusion, Mater. Sci. Eng. A 814 (2021) 141214.

[11] H. Eskandari Sabzi, X. Li, C. Zhang, H. Fu, D. San-Martín, P.E.J. Rivera-Díaz-del Castillo, Deformation twinning-induced dynamic recrystallization during laser powder bed fusion, Scr. Mater. 207 (2022) 114307.

[12] X. Wang, J.A. Muñiz-Lerma, O. Sanchez-Mata, M. Attarian Shandiz, N. Brodusch, R. Gauvin, M. Brochu, Characterization of single crystalline austenitic stainless steel thin struts processed by laser powder bed fusion, Scr. Mater. 163 (2019) 51–56.

[13] S. Scheriau, Z. Zhang, S. Kleber, R. Pippan, Deformation mechanisms of a modified 316 L austenitic steel subjected to high pressure torsion, Mater. Sci. Eng. A 528 (2011) 2776–2786.

[14] S.Gh. Chowdhury, S. Das, P.K. De, Cold rolling behaviour and textural evolution in AISI 316 L austenitic stainless steel, Acta Mater. 53 (2005) 3951–3959.

[15] A. Saeed-Akbari, A. Schwedt, W. Bleck, Low stacking fault energy steels in the context of manganese-rich iron-based alloys, Scr. Mater. 66 (2012) 1024–1029.

[16] H. Eskandari Sabzi, A. Zarei-Hanzaki, H.R. Abedi, R. Soltani, A. Mateo, J.J. Roa, The effects of bimodal grain size distributions on the work hardening behavior of a transformation-twinning induced plasticity steel, Mater.Sci. Eng. A. 678 (2016) 23–32.

[17] Ch. Wang, X. Lin, L. Wang, Sh. Zhang, W. Huang, Cryogenic mechanical properties of 316 L stainless steel fabricated by selective laser melting, Mater. Sci. Eng. A 815 (2021) 141317.

[18] D. Kong, C. Dong, X. Ni, Z. Liang, C. Man, X. Li, Hetero-deformation-induced stress in additively manufactured 316 L stainless steel, Mater. Res. Lett. 8 (2020) 390–397.

[19] Q. Liu, G. Wang, Ch. Qiu, On the role of dynamic grain movement in deformation and mechanical anisotropy development in a selectively laser melted stainless steel, Addit. Manuf. 35 (2020) 101329.

[20] J. Li, M. Yi, H. Wu, Q. Fang, Y. Liu, B. Liu, K. Zhou, P.K. Liaw, Fine-grain-embedded dislocation-cell structures for high strength and ductility in additively manufactured steels, Mater. Sci. Eng. A 790 (2020) 139736.

[21] Z. Li, T. Voisin, J.T. McKeown, J. Ye, T. Braun, Ch. Kamath, W.E. King, Y.M. Wang, Tensile properties, strain rate sensitivity, and activation volume of additively manufactured 316 L stainless steels, Int. J. Plast. 120 (2019) 395–410.

[22] Ch. Qiu, M. Al Kindi, A.S. Aladawi, I. Al Hatmi, A comprehensive study on microstructure and tensile behaviour of a selectively laser melted stainless steel, Sci. Rep. 8 (2018) 1–16.

[23] L. Liu, Q. Ding, Y. Zhong, J. Zou, J. Wu, Y. Chiu, J. Li, Z. Zhang, Q. Yu, Z. Shen, Dislocation network in additive manufactured steel breaks strength-ductility trade-off, Mater. Today 21 (2018) 354–361.

[24] A. Arsenlis, D.M. Parks, Crystallographic aspects of geometrically-necessary and statistically-stored dislocation density, Acta Mater. 47 (1999) 1597–1611.

[25] M.F. Ashby, The deformation of plastically non-homogeneous materials, Phil. Mag. 21 (1970) 399–424.

[26] A. Kundu, D.P. Field, Influence of microstructural heterogeneity and plastic strain on geometrically necessary dislocation structure evolution in single-phase and two-phase alloys, Mater. Charact. 170 (2020) 110690.

[27] J. Jiang, T.B. Britton, A.J. Wilkinson, Evolution of dislocation density distributions in copper during tensile deformation, Acta Mater. 61 (2013) 7227–7239.

[28] H. Eskandari Sabzi, N.T. Aboulkhair, X. Liang, X. Li, M. Simonelli, H. Fu, P.E.J. Rivera-Diaz-del Castillo, Grain refinement in laser powder bed fusion: The influence of dynamic recrystallization and recovery, Mater. Des. 196 (2020) 109181.

[29] J.H. Hollomon, Tensile deformation, AIME Trans. 12 (1945) 1–22.

[30] T. Voisin, J. Forien, A. Perron, S. Aubry, N. Bertin, A. Samanta, A. Baker, Y.M. Wang, New insights on cellular structures strengthening mechanisms and thermal stability of an austenitic stainless steel fabricated by laser powder-bed-fusion, Acta Mater. 203 (2021) 116476.

[31] D. Riabov, A. Leicht, J. Ahlström, E. Hryha, Investigation of the strengthening mechanism in 316 L stainless steel produced with laser powder bed fusion, Mater. Sci. Eng. A 822 (2021) 141699.

[32] D. Kumar, G. Shankar, K.G. Prashanth, S. Suwas, Texture dependent strain hardening in additively manufactured stainless steel 316 L, Mater. Sci. Eng. A 820 (2021) 141483.

[33] H. Choo, K. Sham, J. Bohling, A. Ngo, X. Xiao, Y. Ren, P.J. Depond, M.J. Matthews, E. Garlea, Effect of laser power on defect, texture, and microstructure of a laser powder bed fusion processed 316 L stainless steel, Mater. Des. 164 (2019) 107534.

[34] K. Wang, M. Wu, Z. Yan, D. Li, R. Xin, Q. Liu, Microstructure evolution and static recrystallization during hot rolling and annealing of an equiaxed-structure TC21 titanium alloy, J. Alloys Compd. 752 (2018) 14–22.

[35] J.G. Sevillano, An alternative model for the strain hardening of FCC alloys that twin, validated for twinning-induced plasticity steel, Scr. Mater. 60 (2009) 336–339.

[36] M. Calcagnotto, D. Ponge, E. Demir, D. Raabe, Orientation gradients and geometrically necessary dislocations in ultrafine grained dual-phase steels studied by 2D and 3D EBSD, Mater. Sci. Eng. A 527 (2010) 2738–2746.

[37] G. He, T. Peng, B. Jiang, X. Hu, Y. Liu, Yazheng, C. Wu, Recrystallization behavior and texture evolution in low carbon steel during hot deformation in austenite/ferrite region, Steel Res. Int. 92 (2021) 2100047.

[38] Y. Kim, S. Yang, L. Lee, Superior temperature-dependent mechanical properties and deformation behavior of equiatomic CoCrFeMnNi high-entropy alloy additively manufactured by selective laser melting, Sci. Rep. 10 (2020) 1–13.

[39] Y. Liu, Y. Li, Q. Zhu, H. Zhang, X. Qi, J. Wang, P. Jin, X. Zeng, Twin recrystallization mechanisms in a high strain rate compressed Mg-Zn alloy, J. Magnes. Alloys. 9 (2021) 499–504.

[40] S. Ghosh, M. Patnamsetty, M.C. Somani, P. Peura, Characteristics of dynamic softening during high temperature deformation of CoCrFeMnNi high-entropy alloy and its correlation with the evolving microstructure and micro-texture, J. Mater. Res. Technol. 15 (2021) 6608–6623.

[41] W.F. Xu, Y.X. Luo, M.W. Fu, Microstructure evolution in the conventional single side and bobbin tool friction stir welding of thick rolled 7085-T7452 aluminum alloy, Mater. Charact. 138 (2018) 48–55.

[42] E.I. Galindo-Nava, P.E.J. Rivera-Díaz-del Castillo, Understanding martensite and twin formation in austenitic steels: A model describing TRIP and TWIP effects, Acta Mater. 128 (2017) 120–134.

[43] G.Y. Chin, W.F. Hosford, D.R.D.R. Mendorf, Accommodation of constrained deformation in fcc metals by slip and twinning, Proc. R. Soc. Lond. A Math. Phys. Sci. 309 (1969) 433–456.

[44] U.F. Kocks, H. Mecking, Physics and phenomenology of strain hardening: the FCC case, Prog. Mater. Sci. 48 (2003) 171–273.

[45] E.I. Galindo-Nava, P.E.J. Rivera-Díaz-del Castillo, Thermostatistical modelling of hot deformation in FCC metals, Int. J. Plast. 47 (2013) 202–221.

[46] O. Bouaziz, S. Allain, C. Scott, Effect of grain and twin boundaries on the hardening mechanisms of twinning-induced plasticity steels, Scr. Mater. 58 (2008) 484–487.

[47] H. Zhi, C. Zhang, S. Antonov, H. Yu, T. Guo, Y. Su, Investigations of dislocation-type evolution and strain hardening during mechanical twinning in Fe-22Mn-0.6 C twinning-induced plasticity steel, Acta Mater. 195 (2020) 371–382.

[48] B.C. De Cooman, Y. Estrin, S.K. Kim, Twinning-induced plasticity (TWIP) steels, Acta Mater. 142 (2018) 283–362.

[49] O. Bouaziz, N. Guelton, Modelling of TWIP effect on work-hardening, Mater. Sci. Eng. A 319 (2001) 246–249.

[50] D.R. Steinmetz, T. Jäpel, B. Wietbrock, P. Eisenlohr, I. Gutierrez-Urrutia, A. Saeed-Akbari, T. Hickel, F. Roters, D. Raabe, Revealing the strain-hardening behavior of twinning-induced plasticity steels: Theory, simulations, experiments, Acta Mater. 61 (2013) 494–510.

[51] I. Jung, B.C. De Cooman, Temperature dependence of the flow stress of Fe–18 Mn--0.6 C–xAl twinning-induced plasticity steel, Acta Mater. 61 (2013) 6724–6735.

[52] E.S. Puchi Cabrera, High temperature deformation of 316 L stainless steel, Mater. Sci. Technol. 17 (2001) 155–161.

[53] J. Čapek, M. Machová, M. Fousová, J. Kubásek, D. Vojtěch, J. Fojt, E. Jablonská, J. Lipov, T. Ruml, Highly porous, low elastic modulus 316 L stainless steel scaffold prepared by selective laser melting, Mater. Sci. Eng. C. 69 (2016) 631–639.

[54] C. Robertson, M.C. Fivel, A. Fissolo, Dislocation substructure in 316 L stainless steel under thermal fatigue up to 650 K, Mater. Sci. Eng. A 315 (2001) 47–57.

[55] L.M. Headings, K. Kotian, M.J. Dapino, Speed of sound measurement in solids using polyvinylidene fluoride (PVDF) sensors, Am. Soc. Mech. Eng. 56031 (2013) V001T04A012.

[56] A. Ascari, A.H.A. Lutey, E. Liverani, A. Fortunato, Laser directed energy deposition of bulk 316 L stainless steel, Lasers Manuf. Mater. Process. 7 (2020) 426–448.
[57] E.I. Galindo-Nava, P.E.J. Rivera-Díaz-del Castillo, A thermodynamic theory for dislocation cell formation and misorientation in metals, Acta Mater. 60 (2012) 4370–4378.
[58] E.I. Galindo-Nava, J. Sietsma, P.E.J. Rivera-Díaz-del Castillo, Dislocation annihilation in plastic deformation: II. Kocks–mecking analysis, Acta Mater. 60 (2012) 2615–2624.
[59] J.K. Lee, M.H. Yoo, Elastic strain energy of deformation twinning in tetragonal crystals, Metall. Trans. A. 21 (1990) 2521–2530.
[60] D. Lin, L. Xu, H. Jing, Y. Han, L. Zhao, F. Minami, Effects of annealing on the structure and mechanical properties of FeCoCrNi high-entropy alloy fabricated via selective laser melting, Addit. Manuf. 32 (2020) 101058.